Bulletin of the Seismological Society of America, Vol. XX, No. XX, pp. –, – 2017, doi: 10.1785/0120160312

Nonlinear Site Response at KiK-net KMMH16 (Mashiki) and Heavily Damaged Sites during the 2016 M_w 7.1 Kumamoto Earthquake, Japan

by Hiroyuki Goto, Yoshiya Hata, Masayuki Yoshimi, and Nozomu Yoshida

Abstract Damage from severe ground motion occurred in the downtown area of Mashiki in the Kumamoto Prefecture during the 2016 Kumamoto earthquake, Japan; such damage was heavy in the center of the downtown area. Nonlinear site responses for the first shock and mainshock, which occurred on 14 and 16 April 2016, respectively, are important factors that explain why the area was heavily damaged. We analyzed soil nonlinearity using surface and borehole records obtained from the KiK-net KMMH16 (Mashiki) station. From our analysis, we found that *S*-wave velocity models clearly depended on the amplitude of input ground motion. We estimated the strain-dependent shear stiffness and damping ratio to explain this *S*-wave velocity dependence. We conducted equivalent linear analyses at the KMMH16 site, based on a nonlinear model. From these analyses, we concluded that our synthetic surface ground motions agreed well with the observed ones, especially for the *S*-wave amplitudes and phases of the first shock and mainshock noted above. In addition, we performed the same analyses at the TMP3 site, which was actually located within one of the heavily damaged zones. The synthetic motions here also agreed with the observed ones, with differences in spectral accelerations being well explained by our analyses. Our results indicated that soil nonlinearity played a major role in causing the difference of ground motions, thus leading to the heavily damaged zone in the downtown area of Mashiki.

Introduction

A series of earthquakes started to occur on 14 April 2016, immediately affecting a middle portion of Kyushu Island in Japan; the earthquakes were collectively named the 2016 Kumamoto earthquake by the Japan Meteorological Agency (JMA). The first shock, an M_w 6.1 event, occurred on 14 April 2016, at 21:26 Japan Standard Time (JST) (GMT + 09h); the mainshock, an M_w 7.1 event, then occurred on 16 April 2016, at 01:25 JST. Severe structural damage and landslides in the Kumamoto and Aso areas were mostly caused by this mainshock. Approximately 160 fatalities and 8300 heavily damaged buildings were reported in the Kumamoto Prefecture (Cabinet Office, Government of Japan, 2016). Further, peak ground velocities (PGVs) in horizontal components were observed to be over 1 m/s around the fault segments during the mainshock, as shown in Figure 1. According to the seismic intensity measures taken by the JMA, maximum values of seven were observed at the Mashiki town office during both the first shock and mainshock.

Approximately 30% of the heavily damaged buildings in the Kumamoto Prefecture were concentrated in the downtown area of Mashiki. The damaged area formed a narrow band along the east–west (E–W) corridor with an approximate width of 0.5 km along the main street passing through the center of the downtown area (Yamada *et al.*, 2017). A detailed reconnaissance survey operated by the Architectural Institute of Japan found no significant correlations between the damaged area and the various ages of the buildings (National Institute for Land and Infrastructure Management [NILIM], 2016). For example, a few wooden houses built after 2000, when new building codes for wooden frame houses had been in full effect, were heavily damaged in the band (NILIM, 2016).

Two seismic stations are in operation in the area noted above; these two stations are MTO, which is operated by a local government office, and KiK-net KMMH16 (Mashiki), which is operated by the National Research Institute for Earth Science and Disaster Prevention (NIED). Further, Hata, Goto, and Yoshimi (2016) observed strong ground motions during the mainshock at three temporary stations (i.e., TMP1, TMP2, and TMP3), which are depicted in Figures 1 and 2. The KMMH16 station is located north of the damaged area, whereas TMP3 is located at the center of the damaged

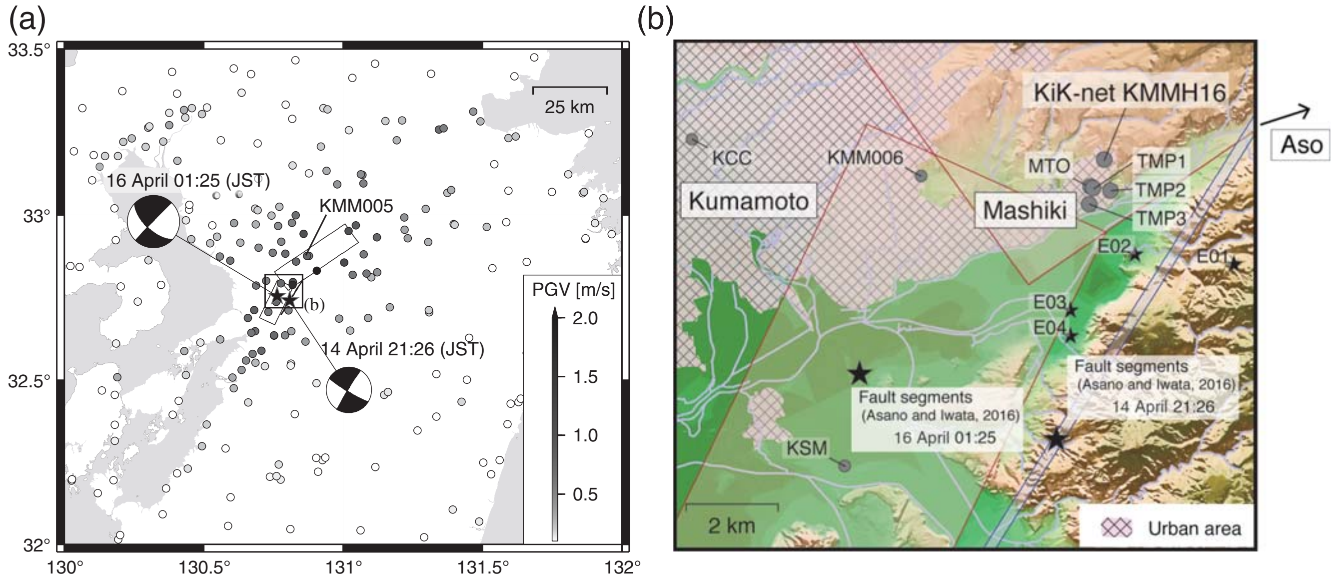

Figure 1. Location of the KiK-net KMMH16 (Mashiki) station and epicenters of the first shock and mainshock during the 2016 Kumamoto earthquake, Japan. (a) Within the rectangles, the stars and the fault mechanisms denote the fault segment, epicenter, and centroid moment tensor solutions during the first shock on 14 April 2016 and the mainshock on 16 April 2016, respectively. The fault segments are referenced from Asano and Iwata (2016). Circles denote the peak ground velocities (PGVs) in horizontal components observed at the K-NET and KiK-net stations, Japan Meteorological Agency (JMA) stations, and seismometers operated by the local government office. (b) Location of temporal seismic stations (TMP1, TMP2, and TMP3) provided by Hata, Goto, and Yoshimi (2016). Stars with notations E01, E02, E03, and E04 denote the epicenters for the selected aftershocks (see Table 2). Rectangles also denote the fault segments. The netted pattern area denotes urban area. JST, Japan Standard Time. The color version of this figure is available only in the electronic edition.

area. At the TMP3 station, 1.82 m/s of PGV and 50.2 m/s^2 of spectral acceleration (SA) at 1.0 s of the natural period were observed, and these values were larger than those at the KMMH16 station (i.e., 1.40 m/s of PGV and 23.7 m/s^2 of SA). These differences in ground motions may have caused the damage distribution in the downtown area of Mashiki.

Spatial differences in ground motion have been observed in several historical earthquakes, in many cases causing a hotspot of structural damage. During the 1995 Kobe earthquake, damage was concentrated in the southern part of the Hyogo Prefecture. Kawase (1996) simulated large PGVs in the damaged area and concluded that the reason for the extensive damage was a focusing of seismic waves due to the 3D subsurface structure. Goto *et al.* (2005) simulated the 3D seismic-wave propagation for the 1999 Kocaeli, Turkey, earthquake, concluding that the 3D subsurface structure explained the concentration of damage in Adapazari. Goto and Morikawa (2012) investigated localized structural damage in the Furukawa district, Miyagi, Japan, after the 2011 Tohoku earthquake by conducting field surveys; further, Goto *et al.* (2012) directly observed ground-motion differences from aftershock records in the area. Other related research (e.g., Gao *et al.*, 1996; Hartzell *et al.*, 1997, 2016; Graves *et al.*, 1998; Galetzka *et al.*, 2015; Takai *et al.*, 2016) concluded that differences in site conditions were important factors in explaining the spatial differences of ground motion. As discussed in Goto *et al.* (2017), a subkilometer-scale variation of ground motions is controlled by the variation of shallow subsurface structure. Therefore, in this article, we attempt to investigate the ground-motion differences at the KMMH16 and TMP3 sites from the variation of shallow subsurface structure by considering site conditions and material nonlinearity.

Nonlinear site response originates in stiffness degradation of soil material associated with shear-strain levels, and the effect this has on strong ground motions has been covered in recent studies (e.g., Satoh *et al.*, 1997; Yoshida *et al.*, 2002; Kwok *et al.*, 2008; Martin *et al.*, 2010; Kaklamanos *et al.*, 2013). The stiffness–strain and damping–strain relations, that is, the G–γ and h–γ curves, respectively, model the nonlinear behaviors; however, no experimental results for the G–γ and h–γ curves are available in Mashiki. We, therefore, focused our efforts on the ground-motion records at the KiK-net KMMH16 station, which contains a vertical array consisting of two acceleration sensors on the ground surface and in the borehole at a depth of 252 m. To explain the spectral ratios of the observed records, the velocities at the KMMH16 site varied from weak to strong motions that reflect the soil nonlinearity at the site. As described in this article, we estimated the G–γ and h–γ curves from the velocity degradation and applied nonlinear models to analyze the nonlinear site response at the KMMH16 and TMP3 sites.

Geological Conditions

Mashiki is a town located in the Kumamoto plain, close to the volcanic caldera of Mount Aso. Marine/nonmarine sediment and volcanic deposits related to the activity of Mt. Aso are distributed in the general area of Mashiki (Hosh-

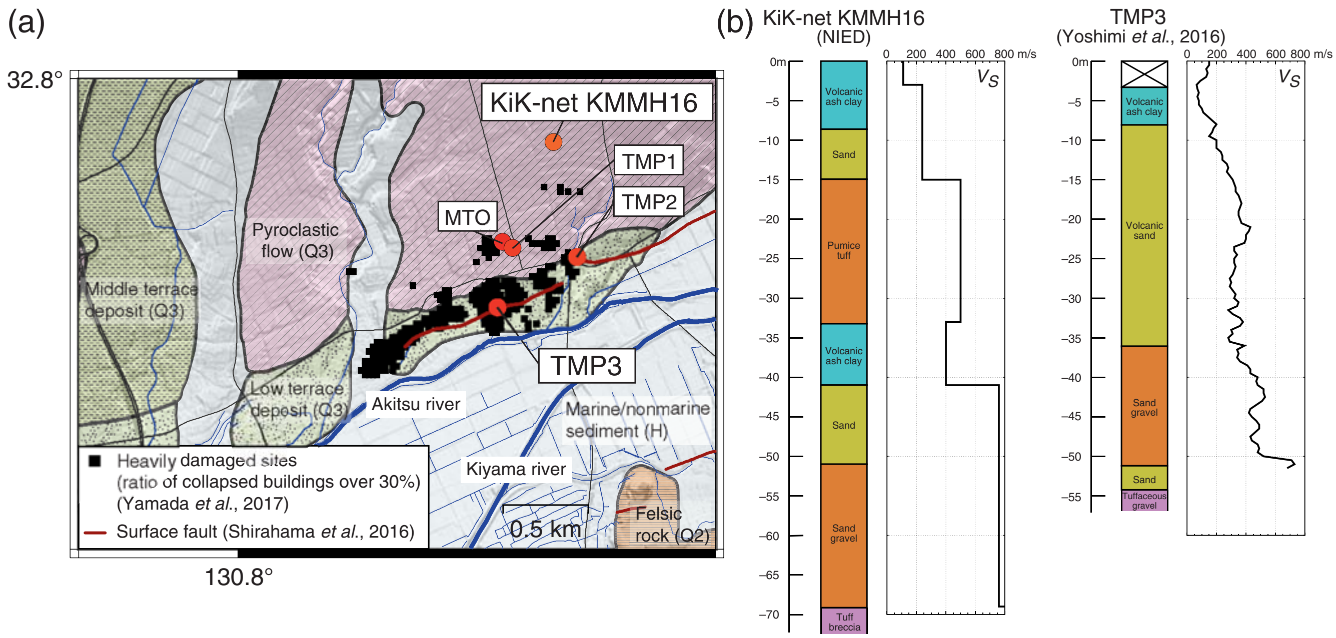

Figure 2. Geological conditions in the downtown area of Mashiki. (a) Geological map provided by the Geological Survey of Japan, AIST (2015) with the locations of seismic stations. Squares indicate heavily damaged zones, defined by a ratio of collapsed buildings over 30% (Yamada *et al.*, 2017). The TMP3 station (Hata, Goto, and Yoshimi, 2016) is located inside the severely damaged area, whereas the KiK-net KMMH16 (Mashiki) station is located outside the damaged area. (b) Soil classifications of the borehole data and the *S*-wave velocity profiles at the KMMH16 site and the sites near the TMP3 site (Yoshimi *et al.*, 2016). NIED, National Research Institute for Earth Science and Disaster Prevention. The color version of this figure is available only in the electronic edition.

izumi *et al.*, 2004). Figure 2 shows the surface geology surrounding the downtown area of Mashiki (geological map by Geological Survey of Japan, Advanced Industrial Science and Technology [AIST], 2015). Low land along the Akitsu and Kiyama rivers are made up of marine/nonmarine sediment from the Holocene. A low terrace deposit of Late Pleistocene forms a narrow band along the northern side of the Akitsu River. A pyroclastic flow of the Late Pleistocene is distributed along the northern border of the area, underlying the MTO and KMMH16 stations. Figure 2 also shows the heavily damaged zones defined by a ratio of collapsed buildings of over 30% (Yamada *et al.*, 2017). The building damage was distributed almost exclusively along the low terrace deposit and not on the marine/nonmarine sediment.

Table 1
Logging Model at the KMMH16 Station [Soil Classification, *S*-Wave and *P*-Wave Velocities (V_S, V_P)]

Soil Classification	V_S (m/s)	V_P (m/s)	Density (kg/m^3)	Damping Ratio	Depth (m)
Volcanic ash clay	110	240	1650	0.03	3
	240	380	1650	0.03	9
Sand	240	380	1700	0.02	15
Pumice tuff	500	1180	1800	0.02	33
Volcanic ash clay	400	1180	1800	0.02	41
Sand	760	1950	2050	0.02	51
Sand gravel					69
Tuff breccia	820	2300	2200	0.02	91
Andesite					97
Tuff breccia					101
Andesite	1470	2800	2200	0.02	133
Tuff breccia	700	2800	2200	0.02	143
Welded tuff	1380	2800	2050	0.02	157
Andesite					169
Tuff	840	2300	2050	0.02	189
Andesite					194
Tuff					201
Andesite	1470	2300	2050	0.02	234
	2700	4800	2500	0	—

Soil stratigraphy at the KMMH16 station was available; we show the upper 70 m of the stratigraphy in Figure 2b and are further listed in Table 1. The stratigraphy here included 9 m of volcanic ash clay underlain by gray sand at a depth of 9–15 m, as well as light gray pumice tuff at a depth of 15–33 m. Sediment at further depths included volcanic ash clay at a depth of 33–41 m and stiffer sand and sand gravel at a depth of 41–69 m underlain by bedrock. Tuff breccia appeared at a depth of 69 m.

Yoshimi *et al.* (2016) conducted core samplings of depth up to 55 m beside the TMP3 station, with a distance of ~10 m. We show this soil stratigraphy in Figure 2b. Volcanic ash clay at a depth of 3–7 m was very soft, whereas volcanic sand at a depth of 7–37 m was light gray and included white pumice stones. The shallower part of the sand gravel at a depth of 37–41 m included more pumice stones, whereas the deeper part of the sand gravel at a depth of 42–51 m was dark gray. Stiff tuffaceous gravel appeared at the bottom of the intermediate layer of sand at a depth of 55 m. *P*–*S*-logging surveys were conducted at the site (Yoshimi *et al.*, 2016), as shown in Figure 2b, but no density profile was available. *S*-wave

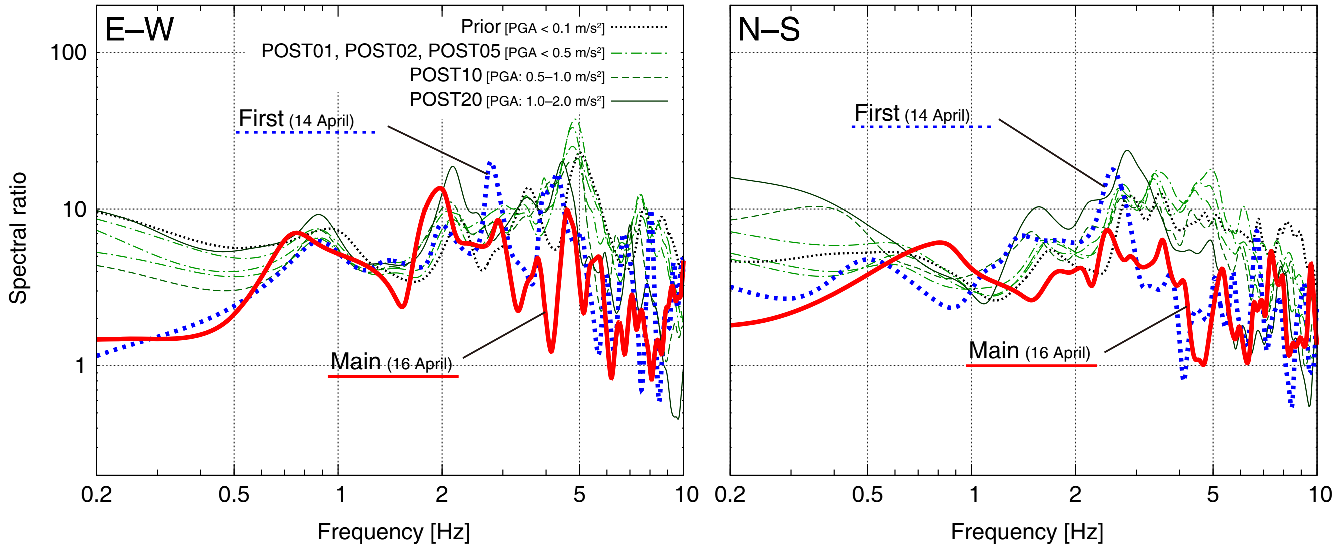

Figure 3. Spectral ratios of the surface-to-borehole records at the KMMH16 station. PRIOR is the average spectral ratios over 25 events prior to the Kumamoto earthquake. POST01, POST02, POST05, POST10, and POST20 are the average spectral ratios for the events during the Kumamoto earthquake sequence, classified into PGAs of the borehole records; 0.05–0.1, 0.1–0.2, 0.2–0.5, 0.5–1.0, and 1.0–2.0 m/s^2, respectively. FIRST and MAIN are the spectral ratios for the first shock and mainshock. E–W, east–west; N–S, north–south. The color version of this figure is available only in the electronic edition.

velocities of 70–80 m/s were measured in shallow layers at a depth of 3–8 m, which gradually increased in the sand layers to ~150–450 m/s to a depth of 37 m. The sand gravel at a depth of 41–50 m showed relatively larger velocities of ~400–800 m/s. Soil stratigraphy, especially the thickness of volcanic sands, differed at the KMMH16 and TMP3 sites. We, therefore, investigated the effect of surface soil on the differences observed in ground motions.

Spectral Ratio of Surface to Borehole Records

At the KMMH16 station in Mashiki, three-component acceleration sensors are installed on the surface and in the borehole at a depth of 252 m. In this section, we first compare the spectral ratio of surface-to-borehole records. An available dataset includes ground-motion records for both a series of the Kumamoto earthquake and events prior to the earthquake. We selected ground-motion records for the first shock, mainshock, and additional events both prior to and during the Kumamoto earthquake events; more specifically, we selected 25 records prior to the first shock and 71 records during the Kumamoto earthquake sequence. Then, we estimated the spectral ratio of surface-to-borehole records for horizontal components for each selected event. Our estimation procedure for obtaining the spectral ratio is as follows:

- Step 1. Find a time window incorporating direct *S*-wave motions. Select the time window of 4.0 s, starting from 1.0 s prior to the moment at which the acceleration in borehole records reaches its maximum.
- Step 2. Multiply the Tukey window (cosine-tapered window, e.g., Harris, 1978) consisting of the 4.0 s of time window by each surface and borehole record.
- Step 3. Calculate Fourier amplitudes for each record and estimate each power spectrum by applying the Parzen window (e.g., Harris, 1978) with a frequency width of 0.4 Hz.
- Step 4. Calculate the square root of the ratio of power spectra (i.e., surface/borehole).

Figure 3 shows the spectral ratio in the E–W and north–south (N–S) components. In this figure, PRIOR indicates the average taken over 25 spectral ratios for events prior to the Kumamoto earthquake. PGAs for all of these 25 records observed in the borehole at a depth of 252 m were less than 0.1 m/s^2. POST01, POST02, POST05, POST10, and POST20 represent the averages taken over the spectral ratios for events during the Kumamoto earthquake sequence classified into PGAs of the borehole data at 0.05–0.1, 0.1–0.2, 0.2–0.5, 0.5–1.0, and 1.0–2.0 m/s^2, respectively. FIRST and MAIN represent the spectral ratios for the first shock and mainshock.

The spectral ratios in the E–W component showed a similar trend among all the events; we observed clear peaks at less than 1, ~2, and 5 Hz. The peak frequency at ~2 Hz gradually shifted to a lower frequency, depending on PGAs of the borehole records. In addition, the peaks at ~5 Hz were smaller during the FIRST and MAIN events than they were during the PRIOR and POST events. Overall, these results indicate the nonlinear response of the surface ground. The spectral ratios in the N–S component showed larger variations, especially for the MAIN event, which differed from the other curves; here, the ground motion may have been affected by the 3D subsurface structure in the Mashiki area, and the structure may cause the spectral ratio variation, depending on the incident angle and azimuth of seismic waves. On the other hand, two strong pulses, which were commonly observed at KiK-net

KMMH16 and TMP1, TMP2, and TMP3 stations, were induced by *S* waves vertically propagating through the surface layer, as discussed in Appendix A. Although we do not have enough knowledge to explain these facts without contradiction at this time, the effect of 3D structure was not dominant, at least for the major pulse in the E–W component. Further, the polarity of the major phase of ground motion during the mainshock was almost entirely in the E–W direction (see Fig. A2), which is significantly important in discussing the cause of the ground-motion damages. Thus, we focused on the E–W components of the ground motion and assumed 1D wave propagation at the sites.

Optimized Velocities and Nonlinear Soil Model at the KMMH16 Site

Verification of Velocity Logging Data

NIED provides borehole data with *P*- and S-wave velocity profiles estimated from *P*–*S*-logging surveys at the KMMH16 station, which we summarize in Table 1. Because the density profile is not available for Mashiki, we refer to the density profiles at the nearby K-NET KMM005 and KMM006 stations. We compared the soil types (e.g., volcanic ash clay) and colors of soil stratigraphy at the KMMH16 site with the soil at the KMM005 and KMM006 sites; as such, we adopted the density of the similar types of soil. Because soil stratigraphy data at the KMM005 and KMM006 sites are available up to a depth of 20 m, the strategy was limited to the surface soils up to a depth of 69 m. Densities for stiffer soils and rocks at a depth of 69–255 m refer to empirical relations to *P*-wave velocity (Ludwig *et al.*, 1970; Miura *et al.*, 2005). Hereafter, we refer to this model as the logging model.

We assume vertical propagation of a 1D *SH* wave. The transfer function, which is defined as the ratio of calculated wave motions at the surface to ones at a depth of 252 m, is calculated using the Haskell–Thomson matrix method (Haskell, 1960). The transfer function is smoothed by the Parzen window with a frequency width of 0.4 Hz. Figure 4 shows a comparison between the synthetic transfer function and the observed spectral ratios for weak motions, corresponding to PRIOR, POST01, POST02, POST05, POST10, and POST20. All peak frequencies on the synthetic curve were higher than the observations. Here, the *S*-wave velocities of the logging model are likely larger than the actual *in situ S*-wave velocities, and therefore we revised the velocity models such that the observed spectral ratios are properly explained.

Velocity Models for Weak Motions (POST02, POST05, POST10, and POST20)

We evaluated the *S*-wave velocity models under weak motions, corresponding to observed spectral ratios for POST02, POST05, POST10, and POST20. We assumed that soil nonlinearity appears on an *S*-wave velocity variation, due to amplitude of input ground motions; thus, we used linear 1D *SH*-wave propagation to optimize the velocity models. We describe the model used to explicitly describe this soil nonlinearity in the Derived Nonlinear Model section.

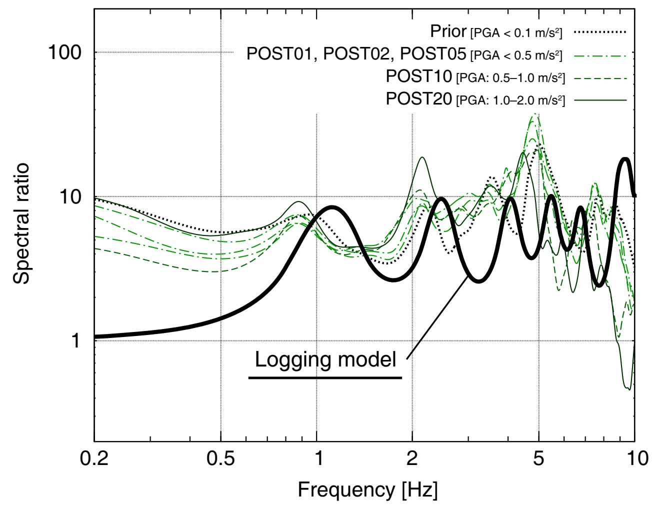

Figure 4. Comparison between the synthetic transfer function from the logging model and the observed spectral ratios for weak motions (PRIOR, POST01, POST02, POST05, POST10, and POST20). The color version of this figure is available only in the electronic edition.

In our analysis, we identified *S*-wave velocities for the first to fifth layers, that is, up to a depth of 41 m. We also set as an unknown variable the ratio of *S*-wave velocity reduction for the sixth to twelfth layers, that is, a depth of 41–234 m. Except for the damping ratios in the POST20 case, the other parameters, including depth, density, and damping ratio, are the same in all cases. The damping ratios of the first to second and third to fifth layers of the POST20 case were set to 0.06 and 0.04, respectively, to explain the decay in the high-frequency range (i.e., 6–8 Hz). Here, the residual norm is defined by the L2 norm on the logarithmic axes within a frequency range of 0.5–8.0 Hz. We applied a genetic algorithm (GA) with 500 members and 200 generations to search for near-optimal values of the six total unknown variables. We examined five trials by changing the seeds of the random numbers independently and then obtained five models for each case.

Figure 5 shows the *S*-wave velocity models for the POST02, POST05, POST10, and POST20 cases, as well as a comparison between the observed spectral ratios and the synthetic ones calculated from each model. Models and spectral ratios for all the five trial cases were plotted together. Velocities in the first to third layers (i.e., a depth of 0–15 m) were almost the same, whereas ones in the fourth to fifth layers (i.e., a depth of 15–41 m) showed relatively large variations. The synthetic spectral ratios showed good agreement with the observed ones, especially for the first and second peaks, though we may need to model more detailed soil layers to represent the third peak. Our results here imply less sensitivity for velocities in the fourth to fifth layers than for velocities in the first to third layers. The *S*-wave velocities in the sixth to twelfth layers were reduced to 75% of the velocities in the

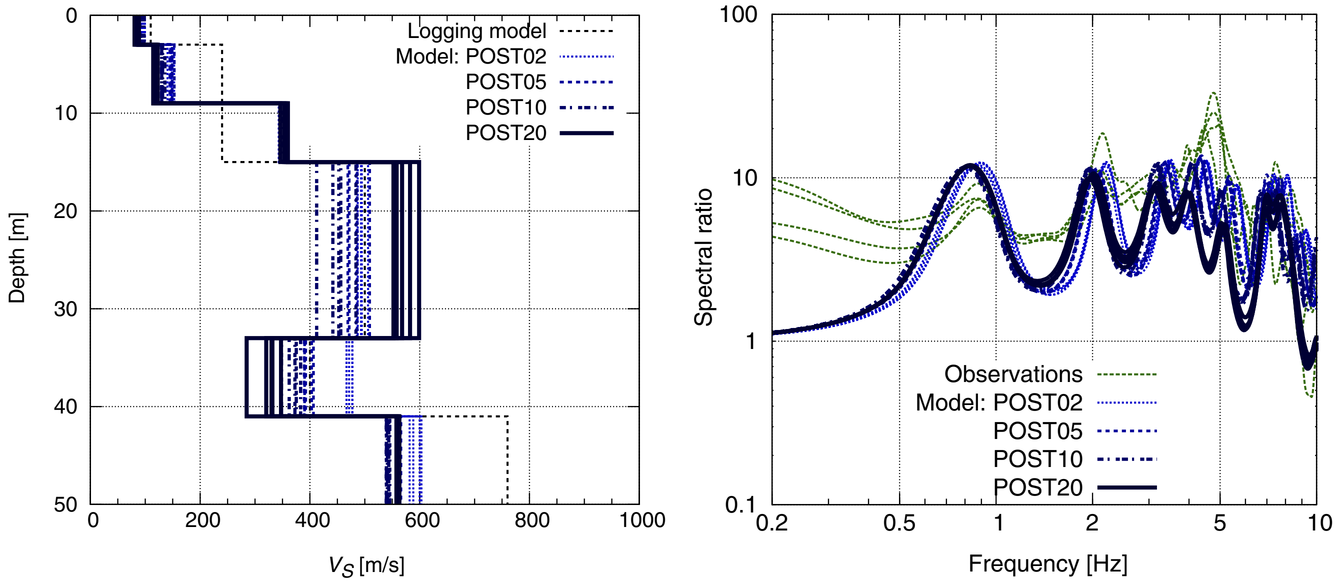

Figure 5. (Left) *S*-wave velocity models to explain POST02, POST05, POST10, and POST20 and (right) comparison between the observed spectral ratios and the synthetic spectral ratios calculated from the models. The color version of this figure is available only in the electronic edition.

logging model, which is seen as a discrepancy in the optimized velocities and logging model at a depth of 41–50 m, as depicted in Figure 5. This result contributes well to fitting the peak frequencies to the synthetic spectral ratios.

Velocity Models for the First Shock and Mainshock

The velocity models for the first shock and mainshock are different because large input ground motion causes a reduction of the *S*-wave velocity, due to the soil nonlinearity. Given this, we optimized the *S*-wave velocity independently for the first shock and mainshock. Here, we applied the same procedure to the datasets corresponding to the first shock and mainshock. As previously mentioned, we used a GA to minimize the residual norms and identify near-optimal values for the six unknown variables, V_S in the first to fifth layers and the V_S reduction ratio for the sixth to twelfth layers; here, the residual norms are defined as the observed spectral ratios for the FIRST and MAIN cases. As shown in Figure 3, on average, the FIRST and MAIN curves showed a rapid decay in the higher frequency range. Goto *et al.* (2013) found that the total damping in surface soil layers controls the frequency average of its transfer function; therefore, we can use the average trend to model the damping ratios. As such, we manually set the damping ratios to 0.15 for the first to second layers and 0.10 for the third to fifth layers.

Figure 6 shows the *S*-wave velocity models for the FIRST and MAIN cases, as well as a comparison between the observed spectral ratios and the synthetic ones calculated from each model. Lower velocities for FIRST and MAIN are clearly estimated in the first to third layers; this phenomenon occurred because of the soil nonlinearity. The synthetic transfer functions explain the peak frequencies at less than 1.0 and ~2.0 Hz. The first and second peak frequencies for the mainshock were lower than the first shock and better fit the observations than the logging model (see Fig. 4). The first peaks were overestimated as being 1.84 times and 1.70 times larger than the observations for the first shock and mainshock, respectively.

Figure 7 shows the synthetic surface ground motions calculated from the borehole records by adopting the optimum velocity models. Arrival time of the *S* wave and its amplitudes were simulated well. Material parameters, such as shear stiffness, were kept constant for each layer in our simulations. Here, shear stiffness must vary, depending on the shear strains at each depth. We created a unified nonlinear model for the KiK-net KMMH16 site and validated it by comparing the result with the observed records.

Derived Nonlinear Model

We estimate the nonlinear soil models from the optimized velocity models obtained in the Velocity Models for the First Shock and Mainshock section. We select six events: the first shock, mainshock, and four shocks that occurred between the first shock and mainshock, as listed in Table 2 (see Fig. 2), and simulate the 1D *SH*-wave propagation applying the borehole records at a depth of 252 m. The velocity models are selected from the corresponding models to PGAs of borehole records. Maximum shear strains at the middle height of every thickness of 1 m are selected, and they are plotted in the diagram of shear stiffness–strain and damping–strain relations.

Figure 8 shows the G–γ and h–γ relationships for the first to fifth layers. The points denote shear stiffness, and the white triangles denote the damping ratios estimated from the velocity models. The squares denote the values estimated from the logging model. The strain dependency on stiffness is

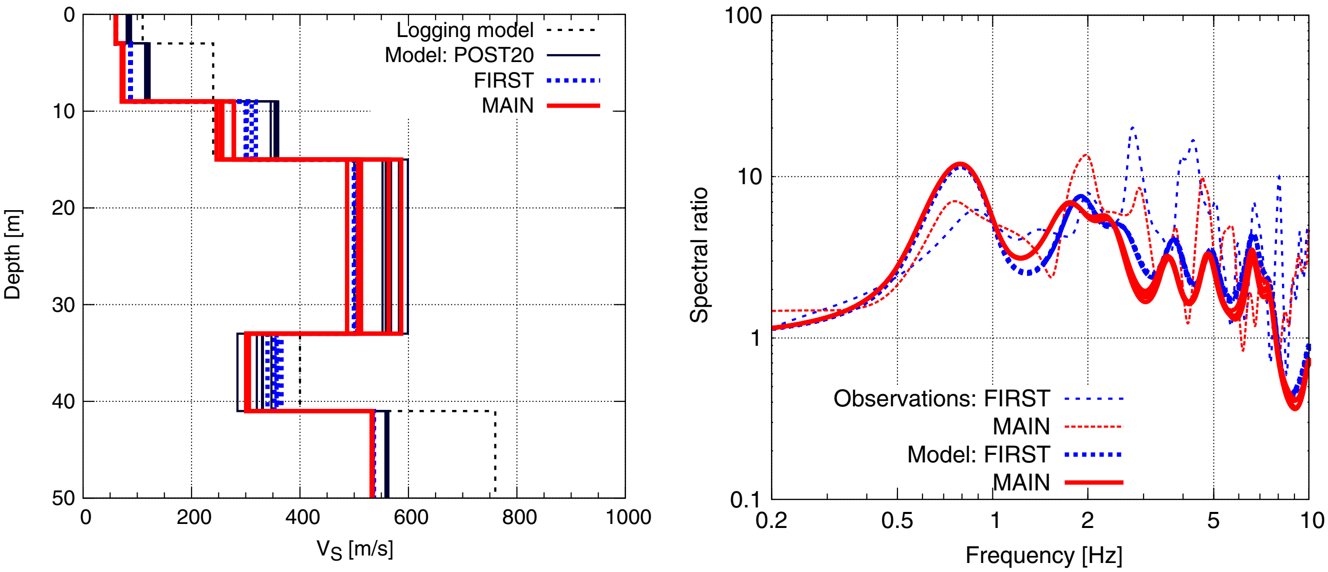

Figure 6. (Left) *S*-wave velocity models to explain the observed spectral ratios for the first shock (FIRST) and mainshock (MAIN) and (right) comparison between the observed spectral ratios and the synthetic spectral ratios calculated from the models. The color version of this figure is available only in the electronic edition.

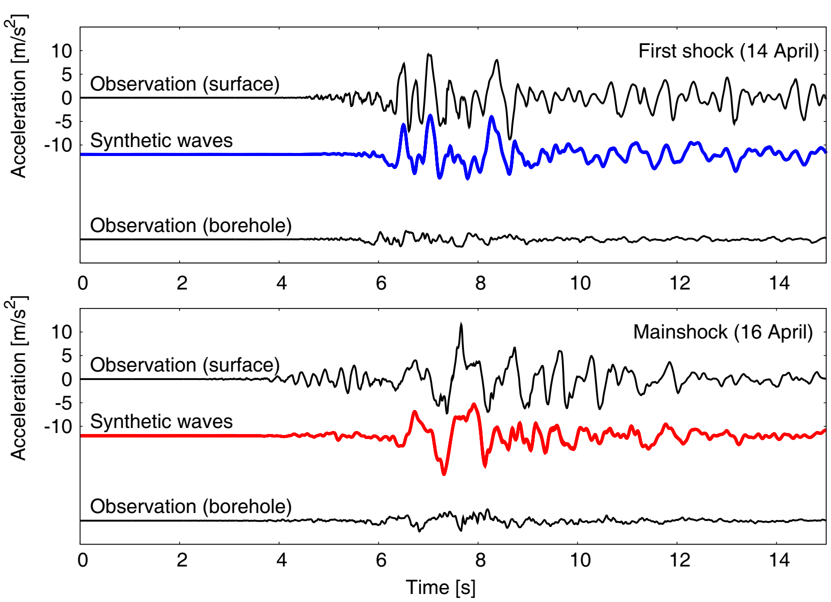

Figure 7. Surface ground motions calculated from the borehole records for the first shock and mainshock by adopting the *S*-wave velocity models. Note that the simulations assume a constant velocity (shear stiffness) in each layer. The color version of this figure is available only in the electronic edition.

clearly seen in each layer, especially for volcanic ash clay (first and second layers, 0–9 m) and sand (third layer, 9–15 m).

The Ramberg–Osgood model (Ramberg and Osgood, 1943; Jennings, 1964) is adopted to model the degradation:

$$\gamma = \frac{\tau}{G_0}\left(1+\alpha\left(\frac{\tau}{\tau_f}\right)^{\beta-1}\right) \quad (1)$$

$$h = \max\left\{\frac{2}{\pi}\frac{\beta-1}{\beta+1}\left(1-\frac{G}{G_0}\right), h_{\min}\right\}, \quad (2)$$

in which τ is the shear stress, and its differentiation of shear strain γ is equal to the shear stiffness G. G_0 is the initial shear stiffness, and α, β, and τ_f are parameters of the Ramberg–Osgood model. In addition, $h_{\min}$ is the minimum threshold to provide a damping ratio under the small strain, as listed in Table 1. The appropriate parameters are manually found to fit the points, as listed in Table 3. Figure 8 also shows the model curves: solid lines denote the G–γ curves, and dashed lines denote the h–γ curves. Both sets of curves represent the points well, especially for the first to third layers. Large variations for Pumice tuff in the fourth layer (15–33 m) resulted, and the model may not represent these well, due to the lower sensitivity in modeling the velocity in the fourth layer.

Nonlinear Site-Response Analysis

KiK-Net KMMH16

Nonlinear site response at the KiK-net KMMH16 (Mashiki) site is calculated by applying equivalent linear analysis. Frequency dependence of the effective strain (Yoshida *et al.*, 2002) is considered in the analysis. The cutoff frequency f_c is 10 Hz. The modeled nonlinear G–γ and h–γ curves for the first to fifth layers are adopted, 75% of the

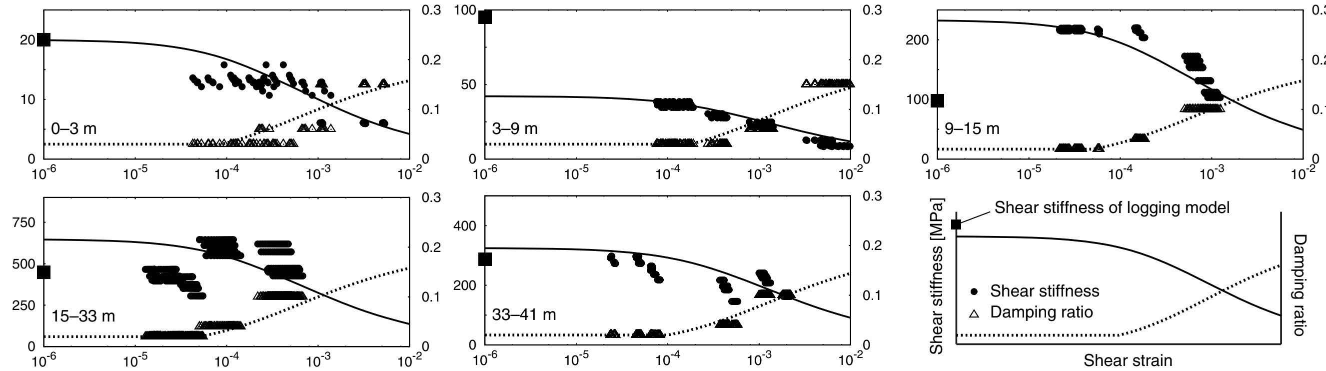

Figure 8. Stiffness–strain and damping–strain relationships for the first to fifth layers (0–41 m in depth) estimated from the velocity models. The points denote shear stiffness, and the white triangles denote the damping ratios estimated from the velocity models. Squares denote the values estimated from the logging model. The solid and dashed lines denote the G–γ and h–γ curves, respectively, represented by the Ramberg–Osgood model (see Table 3).

S-wave velocity relative to the logging model is used for *S*-wave velocities in the sixth to twelfth layers, and they are assumed to maintain linear elastic behaviors. We divide the first to fifth layers (0–41 m) into 1-m-thick layers and do not divide the sixth to twelfth layers (41–252 m).

Figure 9 shows synthetic surface ground motions calculated from the borehole records for the first shock and mainshock. First arrival time, amplitudes, and phase of the *S* waves agree well with the observed records for both the first shock and mainshock. The same analysis is conducted for the four selected aftershocks, as listed in Table 2. The synthetic waves also agree well with the observed waves. Figure 10 shows the distribution of the maximum shear strain and the *S*-wave velocity after all iterations of the equivalent linear analysis. The velocity models (see Fig. 6) are plotted together in the velocity diagrams. The large shear strains appear around 3–9 m in depth, but the magnitudes are less than 1%. The velocity distributions almost follow the models. The spectral ratios of surface-to-borehole motions are compared to the observed spectral ratios. The peak frequencies agree well with the observations, though the amplitudes of the first peak were overestimated for both events. This might suggest revising the physical parameter of the base rock at a depth of 252 m, and that will be discussed in the near future. These results were obtained from a common nonlinear model. They suggest that the model was well validated.

Table 2

Selected Events for Simulating Stiffness–Strain and Damping–Strain Relations and Validation of the Established Model

Event Time (JST, GMT + 09h)	Epicenter	Depth (km)	Strike, Dip, Rake	M_w	Borehole PGA (m/s^2) E–W	Borehole PGA (m/s^2) N–S
14 April at 21:26 (First shock)	N32.742°, E130.809°	11.4	212°, 89°, −164°	6.1	1.78	2.37
14 April at 22:07 (E01)	N32.776°, E130.850°	8.3	293°, 88°, −4°	5.4	0.98	1.68
14 April at 23:29 (E02)	N32.778°, E130.838°	12.8	281°, 73°, −26°	4.4	0.40	0.42
14 April at 23:43 (E03)	N32.767°, E130.827°	14.2	279°, 67°, −22°	4.9	0.28	0.43
15 April at 05:10 (E04)	N32.762°, E130.812°	10.1	278°, 70°, −26°	4.5	0.15	0.18
16 April at 01:25 (Mainshock)	N32.755°, E130.763°	12.4	226°, 84°, −142°	7.1	2.43	1.58

The epicenter locations E01, E02, E03 and E04 are mapped in Figure 2. E–W, east–west; JST, Japan Standard Time; N–S, north–south.

Table 3

Parameters of the Ramberg–Osgood Model

Soil Classification	Initial *S*-Wave Velocity (m/s)	G_0 (MPa)	τ_f (MPa)	α, β	Depth (m)
Volcanic ash clay	110	20.0	0.020	1.887, 1.916	3
	160	42.2	0.085	1.887, 1.916	9
Sand	370	233	0.233	1.887, 1.916	15
Pumice tuff	600	648	0.648	1.887, 1.916	33
Volcanic ash clay	425	325	0.650	1.887, 1.916	41

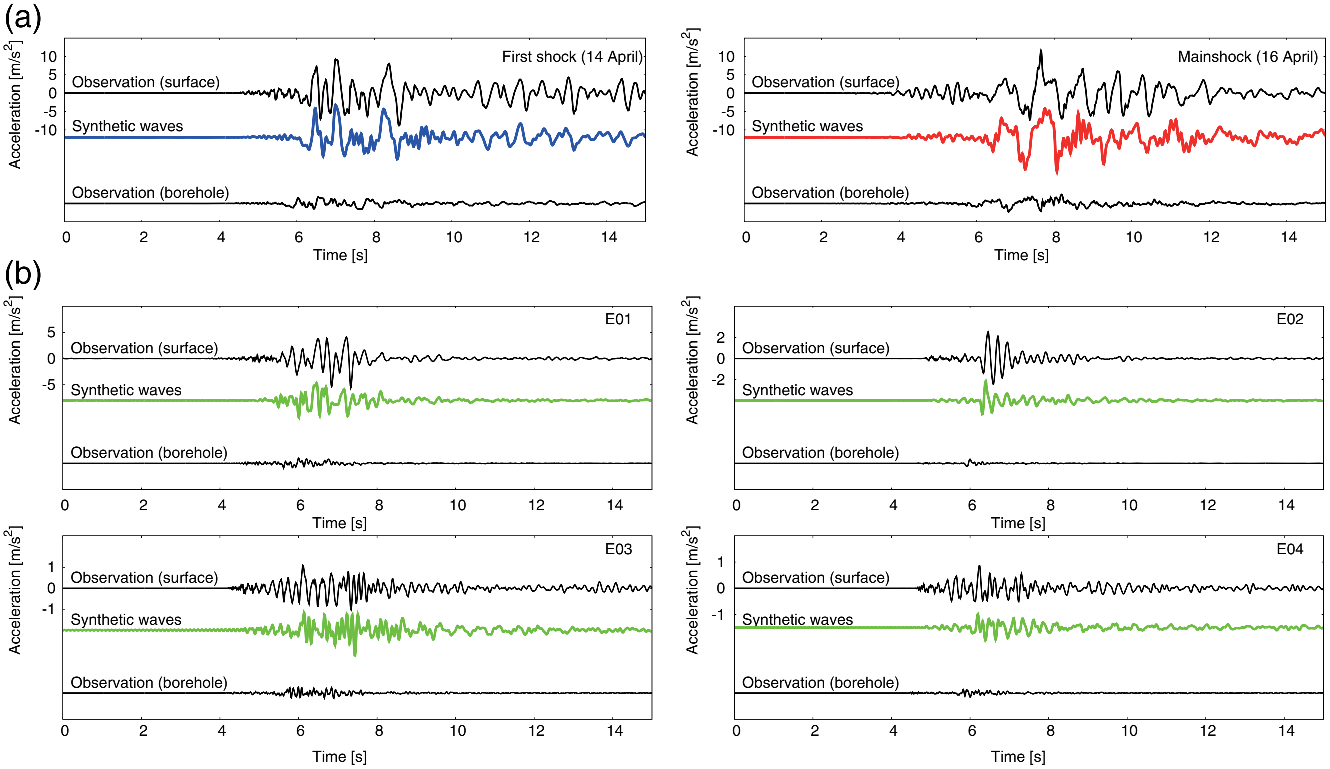

Figure 9. Surface ground motions calculated from the borehole records using equivalent linear analysis, considering soil nonlinearity for the layers at 0–41 m depth. (a) Simulation results for the first shock (14 April 2016) and mainshock (16 April 2016), and (b) for the four selected aftershocks (see Table 2). The color version of this figure is available only in the electronic edition.

TMP3

We examine a nonlinear site-response analysis at the TMP3 site. The nonlinear models for each layer at the KMMH16 site are adopted in modeling the soil nonlinearity at the TMP3 site. Volcanic ash clay up to 7 m (TMP3) is modeled by the nonlinear model of the volcanic ash clay in the first layer at KMMH16. Volcanic sand in 7–37 m (TMP3) is modeled by sand in the third layer at KMMH16, because its color and composite materials are similar. Upper sand gravel at 37–41 m (TMP3) is composed of common white pumice stones as much as is the pumice tuff in the fourth layer at KMMH16 and is associated with the same volcanic event. The *S*-wave velocity of the pumice tuff is estimated to be 400–600 m/s and is similar to the *S*-wave profile of the sand gravel at TMP3. Thus, we assume that the tuff may not be fully consolidated, and the upper sand gravel is modeled by the pumice tuff at KMMH16. Sand and sand gravels at 41–55 m (TMP3) are modeled by the sand and sand gravel in the sixth layer at KMMH16, and it maintains a linear elastic response. The initial *S*-wave velocity model, as listed in Table 3, is almost comparable to the logging data by Yoshimi *et al.* (2016; see Fig. 2b).

The same input motions on tuff breccia (69 m) at KMMH16 and the stiff tuffaceous gravel (55 m) at TMP3 are assumed. Upgoing waves at 69 m for the mainshock are estimated by simulating the equivalent linear analysis at the KMMH16 site, and the wave is input to the boundary at 55 m as the upgoing wave. Figure 11 shows the simulated surface ground motion at TMP3 for the mainshock. The amplitude and phase of the synthetic wave agree well with the observed record. Figure 11 also shows SAs with 5% damping at the KMMH16 and TMP3 stations and their simulated models. The simulated ones at the KMMH16 site are calculated from the waveform, as shown in Figure 9. Both simulated waves at the KMMH16 and TMP3 sites represent the spectral curves well, especially their peak values and peak periods.

Discussions

The difference in ground motions in terms of PGV and SA at 1.0 s was one of the major reasons to form the narrow-damaged band in the downtown area of Mashiki. Hata, Goto, and Yoshimi (2016) used the observed records as evidence for the damaged band.

By assuming that the input ground motions for both KMMH16 and TMP3 sites are identical in these analyses, we used site-response analysis with different soil profiles. This implies that the difference in ground motion comes from the difference of each ground model, such as layer thicknesses. To be clear, we calculate the surface ground motions under the weak input motion, which is 1/100th the amplitude of the original input ground motion during the mainshock.

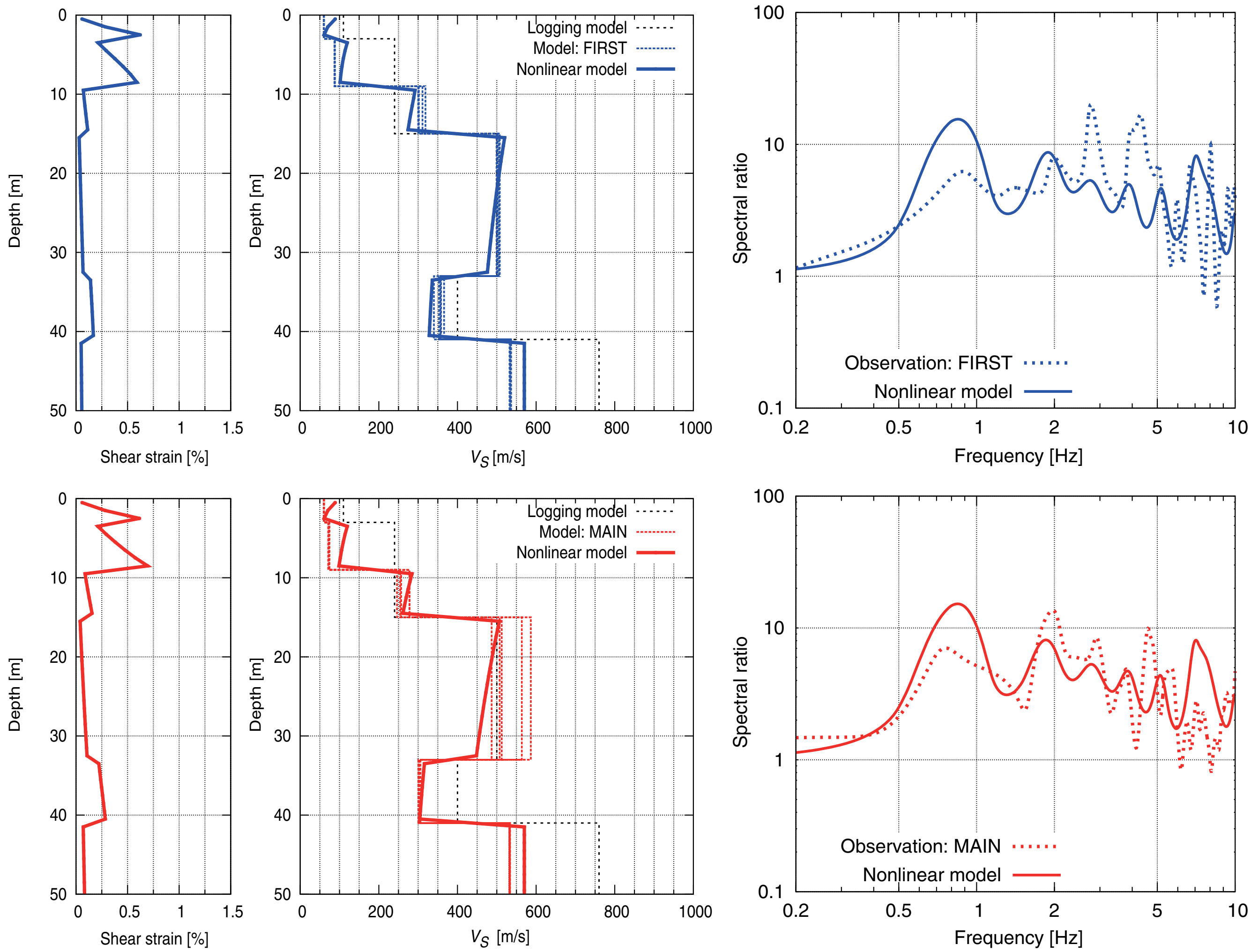

Figure 10. (Left) Maximum shear strain, (middle) *S*-wave velocity profiles, and (right) spectral ratios of surface-to-borehole motions. The top and bottom panels show the results for the first shock and mainshock, respectively. The velocity models (see Fig. 6) are plotted together in the velocity diagram. The color version of this figure is available only in the electronic edition.

Figure 12a shows the calculated surface ground motions at the KMMH16 and TMP3 sites. No clear differences of acceleration response around 1 s are observed. Amplification of the input-to-surface ground motions are compared in Figure 12b. The peaks shift to longer periods differently in the cases of the original input motions. The peak period at the TMP3 site is about 0.85 s, and it could amplify the input ground motion around 1 s.

The actual weak-motion records at the KMMH16 and TMP3 sites are discussed in Appendix B. As seen in the SAs (Fig. B1b), there are no clear differences over 0.3 s of the natural period or even large response for the KMMH16 records in 0.1–0.3 s. In addition, Sugino *et al.* (2016) reported horizontal-to-vertical (H/V) spectral ratios of single-site microtremor observations in the downtown area of Mashiki, and they concluded no clear differences are seen in the H/V spectral ratios between the KMMH16 site and the damaged area around the TMP3 site. The facts are consistent with the results discussed previously and in Figure 12. The amplification could be emphasized under the large input ground motions.

Figure 13 shows the *S*-wave velocity profiles after the equivalent linear analysis iterations for the mainshock and the weak input motion with 1/100th the amplitude of the original one. The *S*-wave velocity at the TMP3 site decreases on average 56% in the clay layer (0–7 m) and 40% in the sand layer (7–37 m), which is larger than the degradation at the KMMH16 site, 33% (0–9 m) and 27% (9–15 m), respectively. Figure 13 also shows the mode shapes at 1.0 Hz close to the peak frequency for the mainshock and at 3.0 Hz close to the peak frequency for the weak motion. Mode shapes are similar for both levels of input motion at 1.0 Hz, and the relative displacement in both the clay and the sand layers is emphasized. This indicates that the soil nonlinearity of both the clay and the sand layers caused velocity degradation during the mainshock, that the peak period shifted to about 1.0 s, and therefore that ground motion was amplified through both layers.

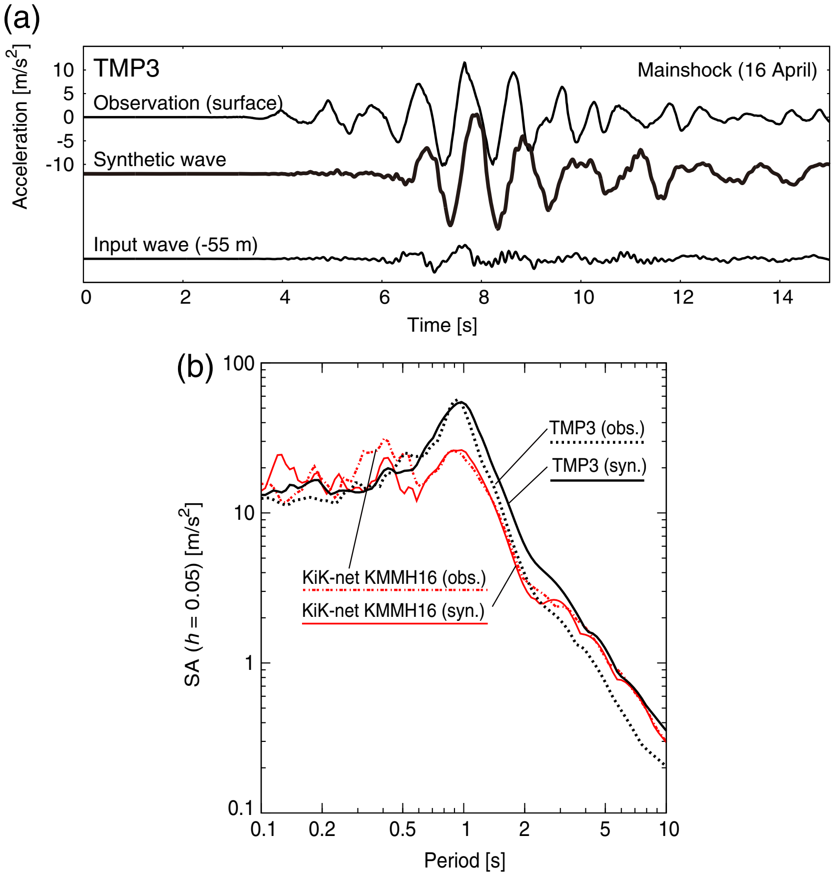

Figure 11. Simulated surface ground motion at the TMP3 site during the mainshock of the 2016 Kumamoto earthquake. (a) Simulated surface ground motion calculated from the input motion at a depth of 55 m, which is estimated at the KMMH16 site. (b) Comparison of spectral accelerations of the observed records and the synthetic records at the KMMH16 and TMP3 sites. SA, spectral acceleration. The color version of this figure is available only in the electronic edition.

Our results show that the surface ground accelerations near the 1 s period at the KMMH16 and TMP3 sites are similar for weak ground motions, but nonlinear effects make them much different during strong ground motions (e.g., Fig. 12). The differences in ground accelerations caused by the soil nonlinearity, which we document here, are the cause of the differences in damage during the strong ground accelerations during the mainshock.

Conclusion and Remarks

We simulated surface ground motions at the KiK-net KMMH16 (Mashiki) station for the first shock and mainshock during the 2016 Kumamoto earthquake. *S*-wave velocity models clearly depended on the amplitude of the input ground motions. Relations of shear stiffness and damping ratio to shear strain were estimated and modeled as G–γ and h–γ curves. We conducted equivalent linear analyses at the KMMH16 site, based on the nonlinear model. The synthetic surface ground motions agreed well with the observed motions, especially for the *S*-wave amplitude and phase for the first shock and mainshock. In addition, we also conducted the same analyses at the TMP3 site, which was in the heavily damaged zones. The synthetic motions well represented the observed motions, and the difference of SAs was well explained by the analyses. The results indicated that the soil nonlinearity played a major role in causing the difference of ground motions, in terms of peak frequency shift to around 1.0 Hz, and thus the damaged zone appeared in the downtown Mashiki.

In this study, we estimated the soil nonlinearity from the observed records at the KMMH16 station. Instead of the estimated G–γ and h–γ curves, undisturbed samplings of the target soils and their laboratory tests, such as the triaxial test and the cyclic shear test, are required for more precise discussion. In addition, more borehole data and geophysical exploration surveys will aid in distinguishing the subsurface structures inside and outside of the narrow-damaged band.

Data and Resources

Strong-motion records and soil stratigraphy were obtained from databases organized by the National Research Institute for Earth Science and Disaster Prevention (NIED; http://www.k-net.bosai.go.jp/, last accessed September 2016), the Japan Meteorological Agency (JMA), the local government office (Kumamoto prefecture), and temporal stations in Mashiki (Hata, Goto, and Yoshimi, 2016; http://wwwcatfish.dpri.kyoto-u.ac.jp/~kumaq/, last accessed September 2016). Event time, epicenter, and depth are referenced from the JMA Unified Hypocenter Catalogs by Hi-net website (NIED; http://www.hinet.bosai.go.jp, last accessed September 2016), and strike, dip, rake, and M_w are referenced from the F-net website (NIED; http://www.fnet.bosai.go.jp, last accessed September 2016). Nonlinear site responses were calculated using the DYNEQ computer program (http://www.civil.tohoku-gakuin.ac.jp/yoshida/computercodes/, last accessed September 2016).

Acknowledgments

The authors thank Thomas Pratt and anonymous reviewers for their fruitful comments. The authors also thank organizations for providing strong-motion records: K-NET and KiK-net operated by National Research Institute for Earth Science and Disaster Prevention (NIED), Japan Meteorological Agency (JMA), and the local government office. This research was supported by Grants-in-Aid for Scientific Research, Japan Society for the Promotion of Science (JSPS KAKENHI) Grant Number 25709039 and special research fund for collaborative research in Disaster Prevention Research Institute (DPRI), Kyoto University (28U-05 and 28U-07).

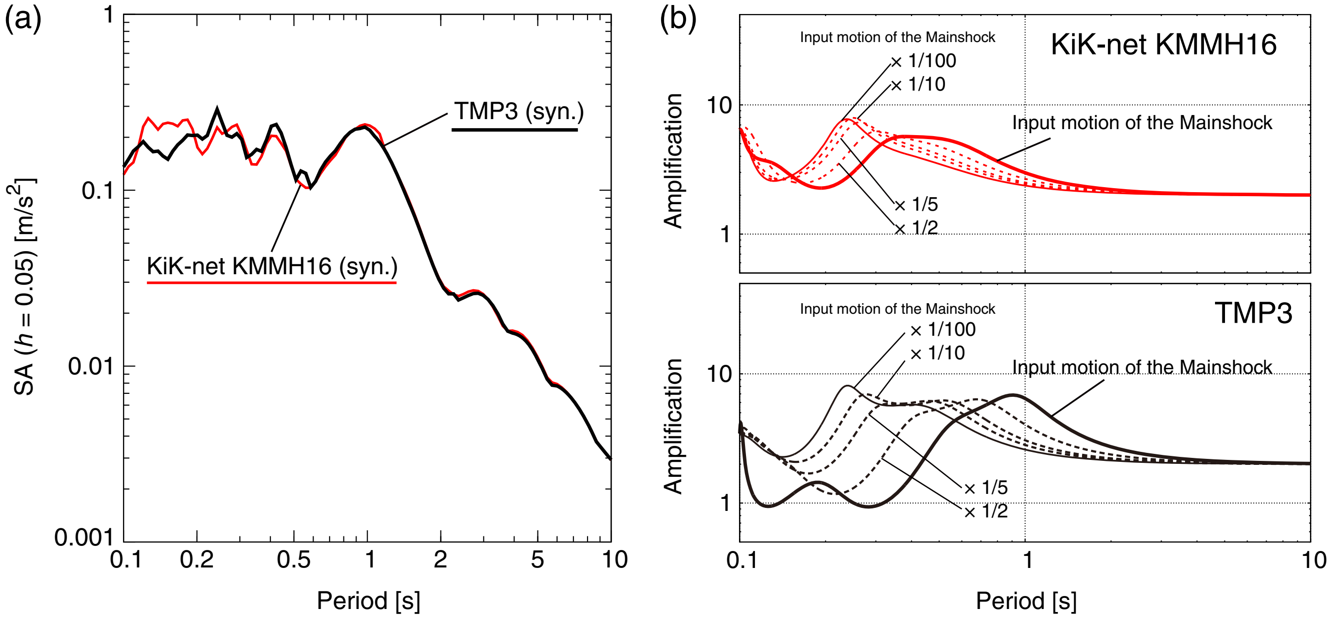

Figure 12. Simulation results for the weak input motion, which is 1/100th the amplitude of the original input motion for the mainshock. (a) Comparison of the spectral accelerations at the KMMH16 and TMP3 sites simulated under the weak input motion. (b) Amplification of the input-to-surface ground motions at the KMHH16 and TMP3 sites for both original and weak input motions. The color version of this figure is available only in the electronic edition.

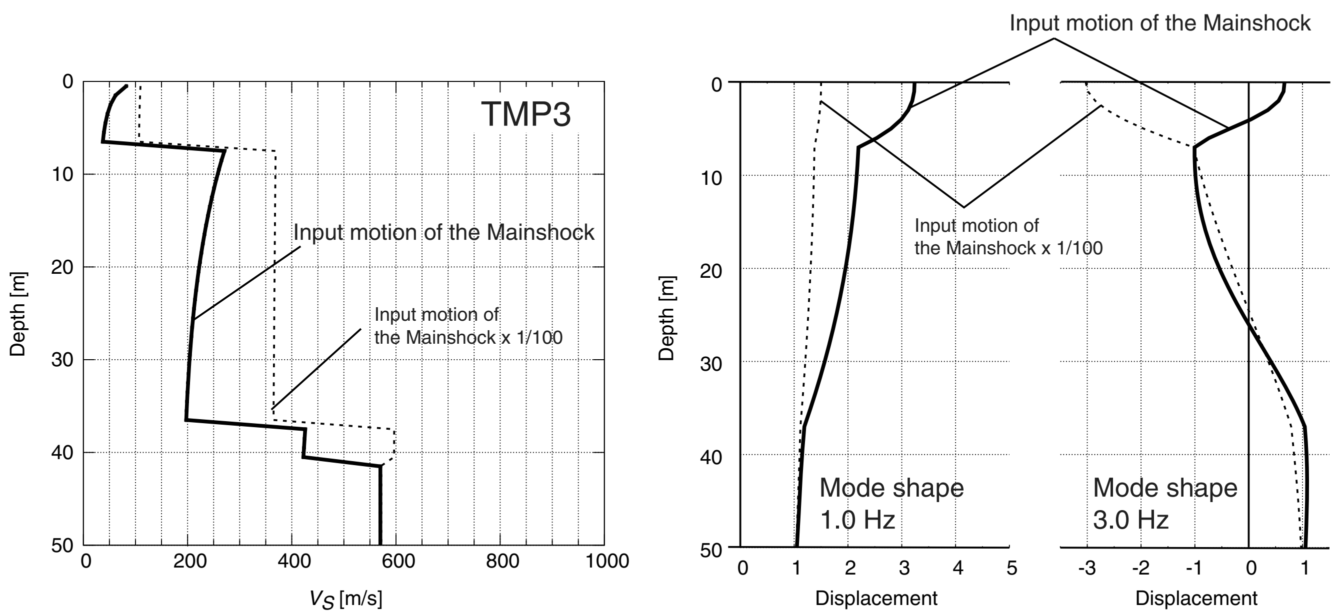

Figure 13. (Left) S-wave velocity profiles for the mainshock and weak input motion (1/100th the amplitude of the original input motion) and (right) the mode shapes for both cases at 1.0 and 3.0 Hz.

References

Asano, K., and T. Iwata (2016). Source rupture processes of the foreshock and mainshock in the 2016 Kumamoto earthquake sequence estimated from the kinematic waveform inversion of strong motion data, *Earth Planets Space* **68,** no. 147, doi: 10.1186/s40623-016-0519-9.

Cabinet Office, Government of Japan (2016). *Damage Situation Associated with the 2016 Kumamoto Earthquake (Dec. 14, 2016)*, Cabinet Office, Government of Japan, available at http://www.bousai.go.jp/updates/h280414jishin/pdf/h280414jishin_37.pdf (last accessed January 2017) (in Japanese).

Galetzka, J., D. Melgar, J. F. Genrich, J. Geng, S. Owen, E. O. Lindsey, X. Xu, Y. Bock, J.-P. Avouac, L. B. Adhikari, *et al.* (2015). Slip pulse and resonance of the Kathmandu basin during the 2015 Gorkha earthquake, Nepal, *Science* **349,** no. 6252, 1091–1095.

Gao, S., H. Liu, P. M. Davis, and L. Knopoff (1996). Localized amplification of seismic waves and correlation with damage due to the Northridge earthquake: Evidence for focusing in Santa Monica, *Bull. Seismol. Soc. Am.* **86,** no. 1B, S209–S230.

Geological Survey of Japan, Advanced Industrial Science and Technology (AIST) (2015). Seamless digital geological map of Japan, Geological Survey of Japan, National Institute of Advanced Industrial Science and Technology, scale 1:200,000.

Goto, H., and H. Morikawa (2012). Ground motion characteristics during the 2011 off the Pacific coast of Tohoku earthquake, *Soils Found.* **52,** no. 5, 769–779.

Goto, H., Y. Kawamura, S. Sawada, and T. Akazawa (2013). Direct estimation of near-surface damping based on normalized energy density, *Geophys. J. Int.* **194,** no. 1, 488–498.

Goto, H., H. Mitsunaga, M. Inatani, K. Iiyama, K. Hada, T. Ikeda, T. Takaya, S. Kimura, R. Akiyama, S. Sawada, *et al.* (2017). Shallow subsurface structure estimated from dense aftershock records and microtremor observation in Furukawa district, Miyagi, Japan, *Explor. Geophys.* **48,** no. 1, 16–27.

Goto, H., H. Morikawa, M. Inatani, Y. Ogura, S. Tokue, X. R. Zhang, M. Iwasaki, M. Araki, S. Sawada, and A. Zerva (2012). Very dense seismic array observations in Furukawa district, Japan, *Seismol. Res. Lett.* **83,** no. 5, 765–774.

Goto, H., S. Sawada, H. Morikawa, H. Kiku, and S. Ozalaybey (2005). Modeling of 3D subsurface structure and numerical simulation of strong ground motion in the Adapazari basin during the 1999 Kocaeli earthquake, Turkey, *Bull. Seismol. Soc. Am.* **95,** no. 6, 2197–2215.

Graves, R. W., A. Pitarka, and P. G. Somerville (1998). Ground-motion amplification in the Santa Monica area: Effects of shallow basin-edge structure, *Bull. Seismol. Soc. Am.* **88,** no. 5, 1224–1242.

Harris, F. J. (1978). On the use of windows for harmonic analysis with the discrete Fourier transform, *Proc. IEEE* 66, **no.** 1, 51–83.

Hartzell, S., E. Cranswick, A. Frankel, D. Carver, and M. Meremonte (1997). Variability of site response in the Los Angeles urban area, *Bull. Seismol. Soc. Am.* **87,** no. 6, 1377–1400.

Hartzell, S., A. L. Leeds, L. Ramirez-Guzman, J. P. Allen, and R. G. Schmitt (2016). Seismic site characterization of an urban sedimentary basin, Livermore valley, California: Site response, basin-edge-induced surface waves, and 3D simulations, *Bull. Seismol. Soc. Am.* **106,** no. 2, 609–631.

Haskell, N. A. (1960). Crustal reflection of plane *SH* waves, *J. Geophys. Res.* **65,** 4147–4150.

Hata, Y., H. Goto, and M. Yoshimi (2016). Preliminary analysis of strong ground motions in the heavily damaged zone in Mashiki town, Kumamoto, Japan, during the mainshock of the 2016 Kumamoto earthquake (M_w 7.0) observed by a dense seismic array, *Seismol. Res. Lett.* **87,** no. 5, 1044–1049.

Hata, Y., H. Goto, M. Yoshimi, A. Furukawa, H. Morikawa, T. Ikeda, and T. Kagawa (2016a). Evaluation of empirical site amplification and phase effects in residential land area around Mashiki Town Office based on the temporary earthquake observation with high dense spatial location, *Proc. of the 60th Geotechnical Engineering Symposium, JGS*, Tokyo, Japan, 165–172 (in Japanese with English abstract).

Hata, Y., H. Goto, M. Yoshimi, A. Furukawa, H. Morikawa, T. Ikeda, and T. Kagawa (2016b). Ground motion estimation in residential land area around Mashiki Town Office, Japan, during the main shock of the 2016 Kumamoto earthquake sequence based on very high-dense seismic observation, *Proc. of the 7th Symposium on Disaster Mitigation and Resilience of Infrastructures and Lifeline Systems, JSCE*, Kumamoto, Japan, 7–18 (in Japanese with English abstract).

Hoshizumi, H., M. Ozaki, K. Miyazaki, H. Matsuura, S. Toshimitsu, K. Uto, S. Uchiumi, M. Komazawa, T. Hiroshima, and S. Sudo (2004). Geological map of Japan 1:200,000, Kumamoto, Geological Survey of Japan, NI-52–11.

Jennings, P. C. (1964). Periodic response of a general yielding structure, *J. Eng. Mech. Div.* **90,** no. 2, 131–163.

Kaklamanos, J., B. A. Bradley, E. M. Thompson, and L. G. Baise (2013). Critical parameters affecting bias and variability in site-response analyses using KiK-net downhole array data, *Bull. Seismol. Soc. Am.* **103,** no. 3, 1733–1749.

Kawase, H. (1996). The cause of the damage belt in Kobe: "The basin-edge effect," constructive interference of the direct S-wave with the basin-induced diffracted/Rayleigh waves, *Seismol. Res. Lett.* **67,** no. 5, 25–34.

Kwok, A. O., J. P. Stewart, and Y. M. A. Hashash (2008). Nonlinear ground-response analysis of Turkey flat shallow stiff-soil site to strong ground motion, *Bull. Seismol. Soc. Am.* **98,** no. 1, 331–343.

Ludwig, W. J., J. E. Nafe, and C. L. Drake (1970). Seismic refraction, in *The Sea*, A. Maxwell (Editor), Wiley InterScience, New York, New York, Vol. 4, 53–84.

Martin, F. D., H. Kawase, and A. M. F. Razavi (2010). Nonlinear soil response of a borehole station based on one-dimensional inversion during the 2005 Fukuoka prefecture western offshore earthquake, *Bull. Seismol. Soc. Am.* **100,** no. 1, 151–171.

Miura, S., N. Takahashi, A. Nakanishi, T. Tsuru, S. Kodaira, and Y. Kaneda (2005). Structural characteristics off Miyagi forearc region, the Japan trench seismogenic zone, deduced from a wide-angle reflection and refraction study, *Tectonophysics* **407,** 165–188.

National Institute for Land and Infrastructure Management (NILIM) (2016). *Report of Committee for Causal Analysis of Building Damages during the 2016 Kumamoto Earthquake*, http://www.nilim.go.jp/lab/hbg/0930/text.pdf (last accessed October 2016) (in Japanese).

Neidell, N. S., and M. T. Taner (1971). Semblance and other coherency measures for multichannel data, *Geophysics* **36,** no. 3, 482–497.

Ramberg, W., and W. R. Osgood (1943). Description of stress-strain curves by three parameters, *NACA Technical Note 902*.

Satoh, T., M. Horike, Y. Takeuchi, T. Uetake, and H. Suzuki (1997). Nonlinear behavior of scoria soil sediments evaluated from borehole records in eastern Shizuoka prefecture, Japan, *Earthq. Eng. Struct. Dynam.* **26,** no. 8, 781–795.

Shirahama, Y., M. Yoshimi, Y. Awata, T. Maruyama, T. Azuma, Y. Miyashira, H. Mori, K. Imanishi, N. Takeda, T. Ochi, *et al.* (2016). Characteristics of the surface ruptures associated with the 2016 Kumamoto earthquake sequence, central Kyushu, Japan, *Earth Planets Space* **68,** no. 191, doi: 10.1186/s40623-016-0559-1.

Sugino, M., R. Yamano, S. Kobayashi, S. Murase, S. Ohmura, and Y. Hayashi (2016). Analyses of building damages in Mashiki town in the 2016 Kumamoto earthquake, *J. Japan Assoc. Earthq. Eng.* **16,** no. 10, 69–85 (in Japanese with English abstract).

Takai, N., M. Shigefuji, S. Rajaure, S. Bijukchhen, M. Ichiyanagi, M. R. Dhital, and T. Sasatani (2016). Strong ground motion in the Kathmandu valley during the 2015 Gorkha, Nepal, earthquake, *Earth Planets Space* **68,** no. 10, doi: 10.1186/s40623-016-0383-7.

Yamada, M., J. Ohmura, and H. Goto (2017). Building damage analysis in the Mashiki town for the 2016 Kumamoto earthquakes on April 14 and 16, *Earthq. Spectra* (in press).

Yoshida, N., S. Kobayashi, I. Suetomi, and K. Miura (2002). Equivalent linear method considering frequency dependent characteristics of stiffness and damping, *Soil Dynam. Earthq. Eng.* **22,** 205–222.

Yoshimi, M., Y. Hata, H. Goto, T. Hosoya, S. Morita, and T. Tokumaru (2016). Boring exploration result in Kumamoto-ken Mashiki-machi, *Proc. of Fall Meeting, Japanese Society for Active Fault Studies*, P-17, 33–34 (in Japanese).

Appendix A

Array Analysis of the Mainshock Records

Velocity waveforms observed in the Mashiki town show two clear strong pulses (see Fig. A1). One appears around 13.5 s in the east–west (E–W) components, and the other around 15.7 s in north–south (N–S) components. Figure A2 shows the trajectories of particle velocity in the time interval of 13.0–14.0 and 15.2–16.2 s in the N–S to E–W planes at

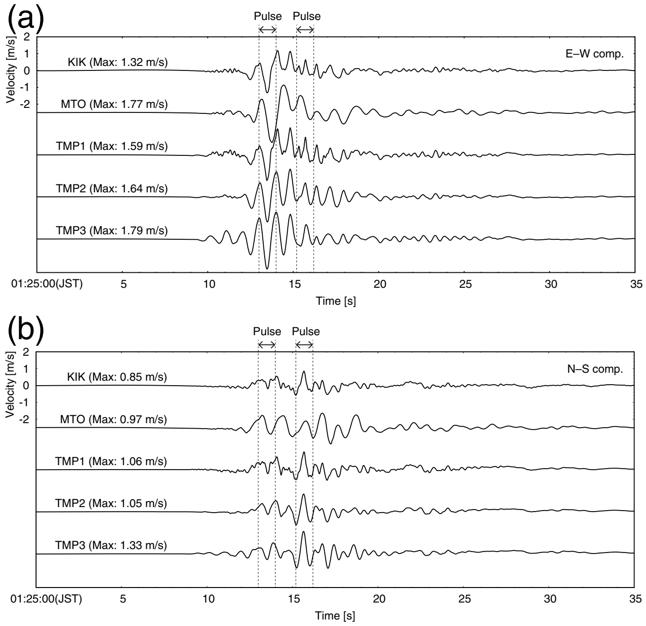

Figure A1. Velocity waveforms at TMP1, TMP2, and TMP3 together with those at permanent stations KIK and MTO during the mainshock for the (a) east–west (E–W) and (b) north–south (N–S) components (Hata, Goto, and Yoshimi, 2016). JST, Japan Standard Time. The color version of this figure is available only in the electronic edition.

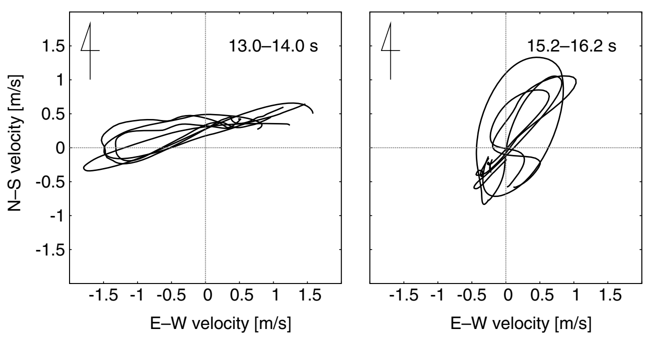

Figure A2. Trajectories of particle velocity in the time interval of (left) 13.0–14.0 s and (right) 15.2–16.2 s in the N–S to E–W plane at KIK, TMP1, TMP2, and TMP3. The color version of this figure is available only in the electronic edition.

KMMH16 (KIK), TMP1, TMP2, and TMP3. The former time interval contains the first strong pulse, and the latter contains the second strong pulse. The first significant motion is mainly oriented in the E–W direction in this time interval. The second significant motion is mainly oriented in the N–E direction in this time interval, which is different from the 13.0–14.0 s time interval.

We calculated semblance values (e.g., Neidell and Taner, 1971) as a function of slowness vector for these two different time intervals. Figure A3 shows the distribution of semblance value for the time interval of 13.0–14.0 and 15.2–16.2 s of the acceleration waveforms at the four stations. We assume that the analysis is accurate up to the apparent phase velocity of 4 km/s because, for the apparent phase velocity of 4 km/s, the maximum time lag within the array corresponds to 0.07 s, that is, seven samples. As indicated in Figure A3, the peak of the semblance value can be found within the concentric circle with the radius of 4 km/s. Although the detailed value of the apparent phase velocity is not estimated, it must exceed 4 km/s. Thus, the wavefield is dominated by body waves rather than surface waves. A similar conclusion can be obtained for the 15.2–16.2 s time intervals. The peak of the semblance value can be found again within the concentric circle with the radius of 4 km/s, which suggests the predominance of body waves. This suggests that the incident waves corresponding to the strong pulses are almost vertical.

Appendix B

Weak-Motion Records at the KiK-Net KMMH16 and TMP3 Stations

A few weak motions prior to the mainshock were observed at the TMP3 station (Hata *et al.*, 2016a, b). We show the weak-motion records for the event (N32.781°, E130.846°, M_w 3.6) that occurred on 15 April 2016 at 12:46 and analyzed the nonlinear site response at the TMP3 and KiK-net KMMH16 sites. Figure B1a shows the acceleration records and calculated surface motions at the TMP3 and KiK-net

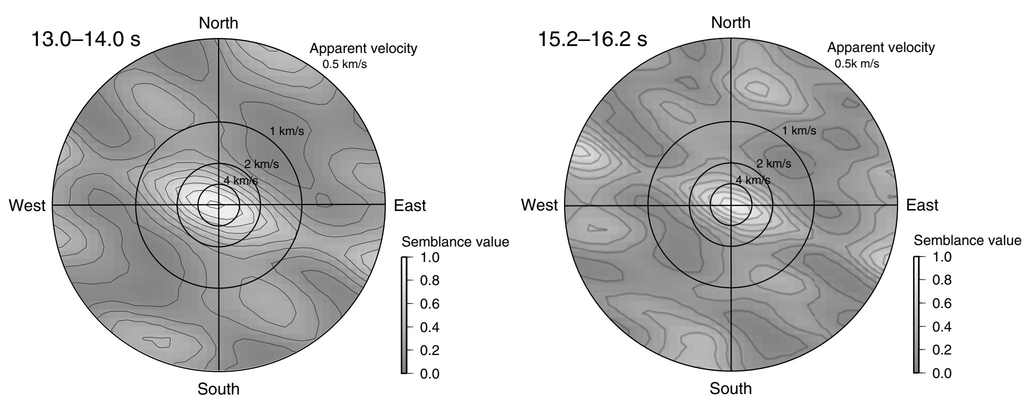

Figure A3. Distribution of semblance values for the time interval of (left) 13.0–14.0 s and (right) 15.2–16.2 s of the acceleration waveforms. The records at KIK, TMP1, TMP2, and TMP3 were used. The concentric circles indicate the apparent phase velocity along the surface. The color version of this figure is available only in the electronic edition.

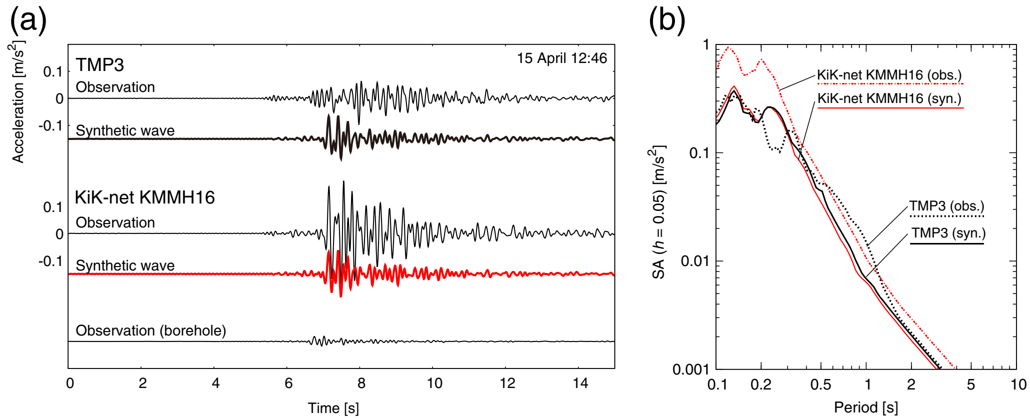

Figure B1. Weak-motion records (15 April at 12:46) at the TMP3 and KiK-net KMMH16 sites. (a) Simulated surface ground motion calculated from the borehole records using equivalent linear analysis. (b) Comparison of spectral accelerations of the observed records and the synthetic models at the KMMH16 and TMP3 sites. SA, spectral acceleration. The color version of this figure is available only in the electronic edition.

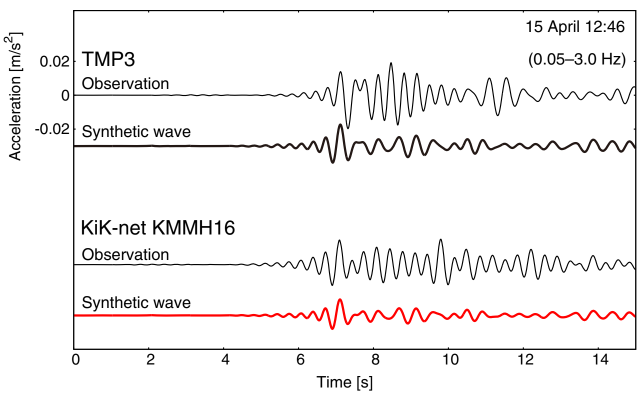

Figure B2. Simulated surface ground motion low-pass filtered up to 3.0 Hz for weak-motion records (15 April at 12:46) at the TMP3 and KiK-net KMMH16 sites. The color version of this figure is available only in the electronic edition.

KMMH16 sites using equivalent linear analysis. Figure B1b shows spectral accelerations with 5% damping. Larger amplitude accelerations were observed at the KiK-net KMMH16 site, which is opposite to the ground-motion damage during the mainshock. The frequency contents of the wake motions, referring to Figure B1b, clearly show the differences emphasized by higher frequency components than 5 Hz. The synthetic waves, shown in Figure B1, do not simulate the records well. One of the main reasons is that our soil model does not guarantee full-frequency bandwidth. As shown in Figures 5–6, the optimized models represent the first and second peak frequencies well, which are less than 3.0 Hz. Thus, the waveforms are low-pass filtered up to 3.0 Hz and are compared in Figure B2. The synthetic waves represent the first arrival of the *S*-waves well at both the KiK-net KMMH16 and TMP3 sites.

Disaster Prevention Research Institute
Kyoto University
Gokasho, Uji
Kyoto 611-0011, Japan
goto@catfish.dpri.kyoto-u.ac.jp
(H.G.)

Graduate School of Engineering
Osaka University
2-1, Yamada-oka, Suita
Osaka 565-0871, Japan
(Y.H.)

Geological Survey of Japan
National Institute of Advanced Industrial Science and Technology
1-1-1, Higashi, Tsukuba
Ibaraki 305-8567, Japan
(M.Y.)

Research Advancement and Management Organization
Kanto Gakuin University
1-50-1, Mutsuura Higashi, Kanazawa-ku
Yokohama 236-8501, Kanagawa, Japan
(N.Y.)

Manuscript received 12 October 2016;
Published Online 4 July 2017